Materials Horizons

ROYAL SOCIETY OF CHEMISTRY

COMMUNICATION

View Article Online
View Journal | View Issue

Check for updates

Cite this: *Mater. Horiz.*, 2022, 9, 383

Received 8th July 2021,
Accepted 17th September 2021

DOI: 10.1039/d1mh01081f

rsc.li/materials-horizons

Crystalline tetra-aniline with chloride interactions towards a biocompatible supercapacitor†

Xiaoling Tong,‡[a] Guan Sheng,‡[b] Dongzi Yang,[a] Shuo Li,[a] Cheng-Wei Lin,[c] Wei Zhang,[d] Zhihui Chen,[a] Chaohui Wei,[a] Xianzhong Yang,[a] Fei Shen,[a] Yanyan Shao,[a] Hui Wei,[a] Yihan Zhu,[b] Jingyu Sun,[ae] Richard B. Kaner*[c] and Yuanlong Shao*[ae]

Recent advances in wearable and implantable electronics have increased the demand for biocompatible integrated energy storage systems. Conducting polymers, such as polyaniline (PANi), have been suggested as promising electrode materials for flexible biocompatible energy storage systems, based on their intrinsic structural flexibility and potential polymer chain compatibility with biological interfaces. However, due to structural disorder triggering insufficient electronic conductivity and moderate electrochemical stability, PANi still cannot fully satisfy the requirements for flexible and biocompatible energy storage systems. Herein, we report a biocompatible physiological electrolyte activated flexible supercapacitor encompassing crystalline tetra-aniline (c-TANi) as the active electrode material, which significantly enhances the specific capacitance and electrochemical cycling stability with chloride electrochemical interactions. The crystallization of TANi endows it with sufficient electronic conductivity (8.37 S cm^{-1}) and a unique Cl$^-$ dominated redox charge storage mechanism. Notably, a fully self-healable and biocompatible supercapacitor has been assembled by incorporating polyethylene glycol (PEG) with c-TANi as a self-healable electrode and a ferric-ion cross-linked sodium polyacrylate (Fe^{3+}-PANa)/0.9 wt% NaCl as a gel electrolyte. The as-prepared device exhibits a remarkable capacitance retention even after multiple cut/healing cycles. With these attractive features, the c-TANi electrode presents a promising approach to meeting the power requirements for wearable or implantable electronics.

New concepts

Conductive polymers have gained extensive attention in the field of wearable energy storage devices due to their tunable molecular structure, accessible solution synthesis, low-cost and biocompatibility. However, synthesizing polyaniline (PANi) with sufficient crystallinity to achieve good electronic conductivity and molecular structural stability is a formidable challenge. Additionally, based on the proton dominated redox active charge storage mechanism of PANi, the acidic electrolyte ruins its inherent biocompatibility. As the smallest structural repeat unit of PANi, tetra-aniline (TANi) can be assembled into ordered nanostructures. Herein, we synthesize highly crystalline TANi (c-TANi) nanosheets as observed *via* low electron dose spherical aberration corrected high-resolution transmission electron microscopy (TEM). Biocompatibility is achieved using an NaCl neutral electrolyte. This creates a unique Cl$^-$ dominated redox charge storage mechanism for c-TANi. The c-TANi electrode exhibits outstanding charge storage capability in a series of physiological electrolytes, including normal saline, phosphate buffered saline (PBS) solution and artificial sweat. A fully self-healable supercapacitor with a c-TANi-PEG electrode and a Fe^{3+}-PANa/0.9 wt% NaCl gel electrolyte has been created for use in biocompatible energy storage applications.

Introduction

Wearable and biocompatible electronics offer a creative platform to bridge artificial intelligent devices with biological tissue for potential applications in health monitoring, remote therapies and clinical disease state evaluation.[1–3] Simultaneously, a boom in wearable and biocompatible electronics has stimulated an ever-growing demand for portable energy storage devices.[4] To satisfy the skin-close or biological application environment, portable energy storage devices should meet a series of extra requirements encompassing safety, flexibility,

---

[a] College of Energy, Soochow Institute for Energy and Materials Innovations (SIEMIS), Key Laboratory of Advanced Carbon Materials and Wearable Energy Technologies of Jiangsu Province, SUDA-BGI Collaborative Innovation Center, Soochow University, Suzhou 215006, P. R. China. E-mail: ylshao@suda.edu.cn

[b] Center for Electron Microscopy State Key Laboratory, Breeding Base of Green Chemistry Synthesis Technology, College of Chemical Engineering, Zhejiang University of Technology, Hangzhou, 310014, P. R. China

[c] Department of Chemistry, Department of Materials Science and Engineering, and California NanoSystems Institute, UCLA, Los Angeles, CA 90095, USA. E-mail: kaner@chem.ucla.edu

[d] State Key Laboratory of Oncogenes and Related Genes, Shanghai Cancer Institute, Renji Hospital, School of Medicine, Shanghai Jiao Tong University, Shanghai 200032, China

[e] Beijing Graphene Institute (BGI), Beijing, 100095, P. R. China

† Electronic supplementary information (ESI) available. See DOI: 10.1039/d1mh01081f

‡ These authors contribute equally to this work.

light-weight and biocompatibility, in addition to appropriate electrochemical performance.[5] Unfortunately, current commercial rechargeable Li-ion batteries or supercapacitors cannot fulfill all these criteria, because of their rigid configurations and hazardous electrolytes including strong acids, bases and flammable organics, thus preventing their incorporation into skin-close or implantable electronics.[6–8] Safety must always be a priority especially for close-fitting or implanted devices. In regard to physiological electrolytes, such as normal saline, sweat, phosphate buffered saline (PBS), and chloride containing compounds (NaCl, KCl) comprise the essential components to sustain living functionality. In this regard, a chloride dominant neutral physiological electrolyte provides a solution to electrolyte safety concerns, while retaining adequate electrochemical performance.[9]

In terms of the electrode material, several pivotal factors, including flexibility and biocompatibility, are still far from satisfactory for most wearable energy storage devices.[10] Conjugated (conducting) polymers, have been broadly demonstrated to be promising candidates for serving as flexible electrodes for biocompatible energy storage devices, according to their intrinsic structural flexibility and polymer chain compatibility with biological tissue.[11,12] Among the conducting polymers, PANi has been considered a very promising candidate for flexible electronics and wearable energy storage devices because of its ultrahigh theoretical specific capacitance (2000 F g^{-1}),[13] facile wet chemical synthesis, confirmed biocompatibility and unique electrochemical activity between its multiple redox states, namely leucoemeraldine-emeraldine and/or emeraldine-pernigraniline.[14] Nevertheless, the long-range disorder inherent in the long polymer chains further hinders efficient charge transport. The limited electronic conductivity and inevitable mechanical degradation tend to trigger severe deterioration of its electrochemical performance and cycling stability.[14–16]

Assembling crystalline structures with conducting polymeric molecules is a promising strategy to tackle these long-standing challenges.[17,18] The structural stability and electronic conductivity can be enhanced by virtue of the compact and ordered polymeric molecular alignment.[19–21] Nevertheless, the complete crystallization of PANi in its long-chain form is immensely challenging due to the unavoidable random coiled conformations triggered by both free energy and kinetic barriers.[11,16,22] As the smallest repeat unit of long-chain PANi, tetra-aniline (TANi) can form into precisely ordered crystalline domains, while preserving most advantages of PANi.[15–17]

Herein, a biocompatible supercapacitor is developed *via* an innovative chloride electrochemical interaction between an elaborate crystalline TANi (c-TANi) electrode and a NaCl dominant physiological electrolyte. The thus-derived c-TANi nanosheets exhibit distinct crystalline domains with highly aligned oligoaniline molecules, which endows it with good electronic conductivity (8.37 S cm^{-1}) and favorable specific capacitance (601 F g^{-1}) *via* chloride dominant redox interactions in an NaCl neutral electrolyte. As such, it far surpasses the corresponding properties of a comparable PANi electrode (1.78 S cm^{-1} and 345 F g^{-1}). A symmetric supercapacitor based on c-TANi electrodes also exhibits an enhanced areal capacitance (414 mF cm^{-2}) with 94.5% capacitance retention even after 4000 cycles in a standard saline solution (0.9 wt% NaCl), which outperforms all previously reported organic electrodes in a physiological electrolyte.[6,8,10,12,23–26] Notably, chloride redox interaction chemistry and the rigid crystalline structure of c-TANi help reinforcing the faradaic charge storage and electrochemical cycling stability, respectively. As a consequence, a fully self-healable and biocompatible quasi-solid-state supercapacitor has been created by incorporating c-TANi-PEG electrodes and ferric ion cross-linked sodium polyacrylate (Fe^{3+}-PANa)/0.9 wt% NaCl gel electrolyte. Such a skillful configurational design enables an areal capacitance of 81.5 mF cm^{-2} and a favorable capacitance preservation of 77.8% even after multiple cut/healing cycles. The c-TANi-PEG//Fe^{3+}-PANa/0.9 wt% NaCl system can successfully power a light-emitting-diode (LED) indicator even after a cut/healing cycle, thus holding great promise for next generation wearable or implantable energy storage devices.

Results and discussion

Fig. 1A schematically illustrates the configuration of the biocompatible supercapacitor, encompassing c-TANi electrodes and an NaCl dominant physiological electrolyte. Note that the c-TANi electrode demonstrates chloride participated redox active interactions, implying appreciable charge storage capability. More encouragingly, the majority of physiological electrolytes, including sweat, urine, blood and normal saline, contain chloride compounds, indicative of directly serving as electrolytes for c-TANi supercapacitors. In this regard, benefiting from the organic features of the electrode materials and physiological electrolyte, the thus-devised c-TANi supercapacitor holds promise for biocompatible energy storage devices for wearable, epidermic or even implantable applications.

The c-TANi nanosheets were prepared *via* a reported solution self-assembly strategy.[15,27] A scanning electron microscopy (SEM) image shown in Fig. S1A (ESI†) reveals the thus-prepared c-TANi with a uniform nanosheet morphology with diameters of ∼1.5 μm and thicknesses of ∼40 nm. The sharp spots in the selected area electron diffraction (SAED) pattern (Fig. S1B, ESI†) provide evidence for the prominent crystallinity with a dominant crystalline peak centered at $2\theta \sim 19.3^\circ$. The peak manifests a *d*-spacing of 0.46 nm corresponding to the peak of 19.3° in the X-ray diffraction pattern (XRD) (Fig. 1B). The predominant π–π stacking *d*-spacing of ∼0.347 nm at 25.6° is perpendicular to the aromatic ring stacking, which corresponds to the TANi molecular assembly.[15,28] We also synthesized PANi as a control sample by means of classical ammonium peroxydisulfate induced polymerization. As displayed in the SEM image (Fig. S1C, ESI†) and XRD (Fig. 1B) profiles, PANi manifests a typical nanofiber morphology and amorphous structure. Matrix-assisted laser desorption/

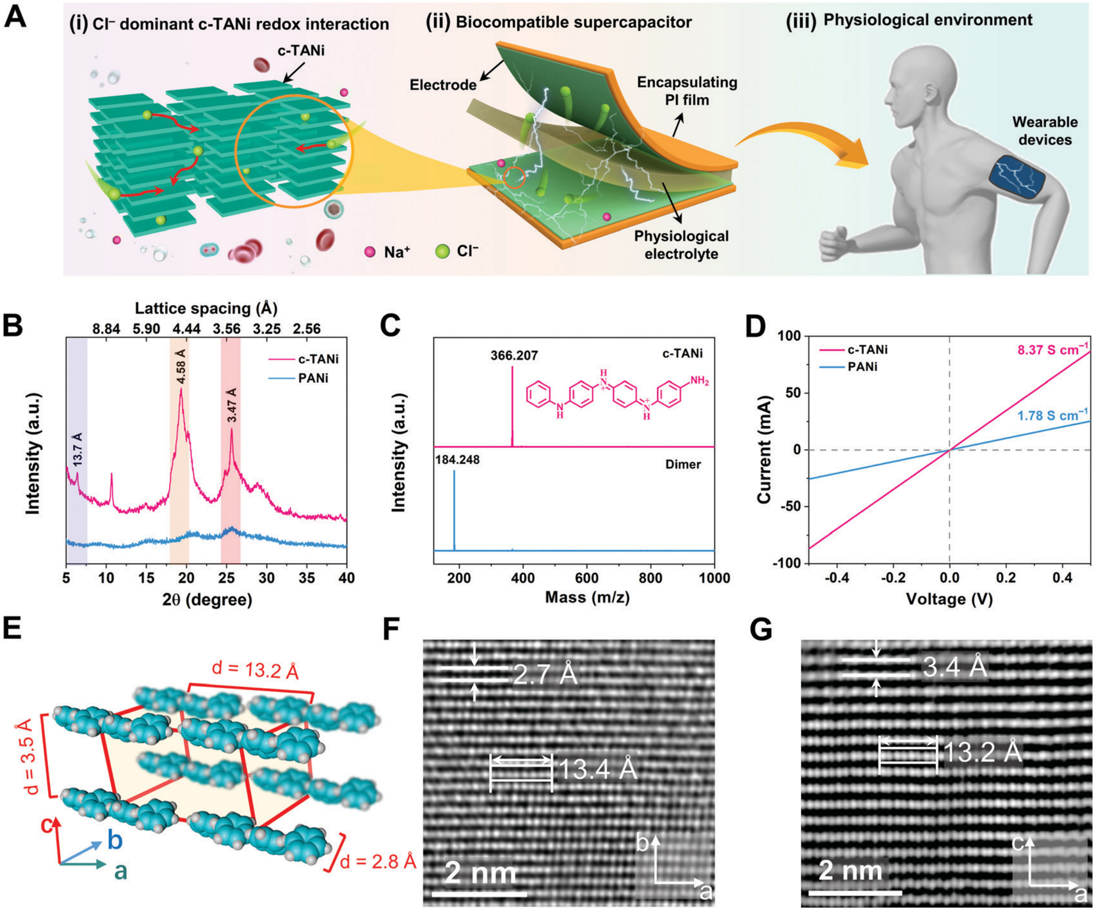

Fig. 1 Schematic illustration of the biocompatible supercapacitor and characterization of c-TANi nanosheets. (A) Configuration of the biocompatible supercapacitor and proof-of-concept demonstration of potential applications. (B) XRD comparison of the c-TANi nanosheets and PANi. (C) MALDI-TOF pattern of the raw dimer material and c-TANi in its emeraldine salt oxidation state. (D) *I*–*V* curves for evaluating the electronic conductivity of c-TANi and regular PANi. (E) The structural illustration of the single unit cell for c-TANi and the packing model of c-TANi chains showing the corresponding lattice spacings and chain stacking along the *a*- and *c*-axis analyzed from the AC-HRTEM results in (F) and (G). AC-HRTEM images of the c-TANi chains along the *a*-axis and (F) π–π stacking of the c-TANi along the *c*-axis (G).

ionization-time-of-flight (MALDI-TOF) mass spectroscopy (Fig. 1C) was employed to characterize the molecular weight of the as-prepared TANi as 366.207 Daltons, completely consistent with the previously reported amine/phenyl-capped TANi.[15,27]

Ultraviolet-visible (UV-vis) spectra (Fig. S1D, ESI†) were used to characterize the doping level and molecular characteristics of doped c-TANi, de-doped TANi and doped PANi. Both doped c-TANi and de-doped TANi display a typical π–π* transition peak at 310 nm.[15] Doped PANi presents a similar peak with a conspicuous red shift, which can be resolved to weaker intermolecular interactions and more distorted π–π stacking that induce lower energy excitonic transitions.[16,29] The broad absorption peak centered at 430 nm suggests a divergence between the doped and de-doped c-TANi, which indicates the polaron to π* band transition.[15] This is the typical indicator for the conductive form of doped c-TANi.

Spherical aberration corrected high-resolution TEM (AC-HRTEM) was used to further characterize the crystalline structure at the sub-nanometer level resolution with an extremely low electron dose rate down to 2 e^- $pixel^{-1}$ s^{-1} to avoid electron beam damage to c-TANi. In comparison to its long-range disordered PANi counterpart, the c-TANi exhibits a highly aligned packing structure with an ordered molecular arrangement, which may be assigned to an orthorhombic lattice, according to the high-resolution TEM images and SAED patterns presented in Fig. 1F and G, Fig. S1B and S2 (ESI†). The typical lattice spacings of 2.7 Å correspond to the opposite (*i.e.* para) position carbon on the aligned aromatic ring along the *b*-axis, while 3.4 Å represents the spacing of the π–π stacking between aromatic planes along the *c*-axis (Fig. 1E).[28] The eight continuous spots with lengths of ~13.5 Å in both Fig. 1F and G represent the stacked aromatic atoms of a single c-TANi molecule along the axial direction of the chain segments. Simultaneously, both the observed 3.4 Å π–π stacking spacing and the single molecular length of 13.5 Å are consistent with the marked peaks in the XRD pattern at 2θ of ~25.6° and 6.4°, which correspond to the lattice spacings of 3.47 Å and 13.7 Å.

Additionally, the lattice spacing of 4.6 Å in Fig. S2G and H (ESI†) matches the peak at 2θ of $\sim$19.3° in the XRD pattern (Fig. 1B).

Consistent with the highly crystalline features, a pressed c-TANi film displays a typical electronic conductivity of 8.37 S cm^{-1} (Fig. 1D), which is approximately four times higher than that of amorphous PANi (1.78 S cm^{-1}). The enhanced conductivity of c-TANi is related to the compact and long-range ordered TANi molecules aligned along the in-plane direction.

The thus-derived c-TANi electrode was subjected to exhaustive electrochemical characterization in a neutral aqueous electrolyte of 2.0 M NaCl *via* a three-electrode cell configuration. Fig. 2A displays the cyclic voltammetry (CV) curve comparison between c-TANi and PANi electrodes performed at a sweep rate of 5 mV s^{-1} within a potential range from −0.2 to 0.6 V *vs.* Ag/AgCl. Generally, the main contribution to the charge storage of PANi is the proton doping/de-doping in an acidic electrolyte, associated with PANi oxidation state variations.[30,31] In this respect, the PANi electrode only displays a moderate electrochemical charge storage capacity with a gravimetric capacitance of 399 F g^{-1}, restricted by the scarcity of protons in the neutral electrolyte. In contrast, benefiting from the redox interactions, the c-TANi electrode achieves a superior specific capacitance of 600.7 F g^{-1} with a consistent discharge rate. The dominant redox reaction around 0.37 V indicates the good redox active charge storage capacity of c-TANi. This trend can also be evidenced by the prolonged diagonal discharge profile of c-TANi at the coincident redox potential range in a galvanostatic charge/discharge (GCD) plot (Fig. S4A, ESI†). The enhanced crystallinity and highly aligned molecular structure imbue c-TANi with ordered ion transport channels for charge storage in comparison to its amorphous PANi counterpart.

Fig. 2B summarizes the specific capacitances of c-TANi and PANi obtained from the CV profiles at varied scan rates. The c-TANi electrode presents a favorable rate performance with 64% capacitance retention when increasing the scan rate from 2 mV s^{-1} to 100 mV s^{-1}, in contrast to a 42% capacitance retention for PANi. Apart from the electronic conductivity, ion dynamics is another vital factor accounting for the differences in electrochemical performance. To unravel the chloride diffusion properties, the *b*-value was calculated on the basis of the equation $i = a\nu^{b}$ by extracting the current from the CV curves performed under different sweep rates (Fig. 2C). The c-TANi and PANi electrodes exhibited *b*-values of 0.89 and 0.81, respectively, indicating a capacitive behavior dominated charge storage process for the c-TANi electrode. Based on *Trasatti*'s theory, the voltametric capacity can be extracted into "outer" capacitive charge and "inner" diffusion controlled redox active behavior dominated charge.[32] We can distinguish these two charge contributions according to the following equation, $i(V) = k_1\nu + k_2\nu^{1/2}$, where $k_1\nu$ and $k_2\nu^{1/2}$ denote the capacitive controlled and diffusion-tailored current contributions, respectively. Fig. 2D summarizes the histogram of the capacitive contributions that originate from the CV curves (Fig. S5A, ESI†) at scan rates from 2 to 20 mV s^{-1}. Accordingly, the capacitive charge contribution ratio of the c-TANi electrode increased from 85.6% to 95.5% as the scan rate increased. The capacitive behavior dominated charge storage mechanism of the c-TANi electrode enables the remarkable rate performance.

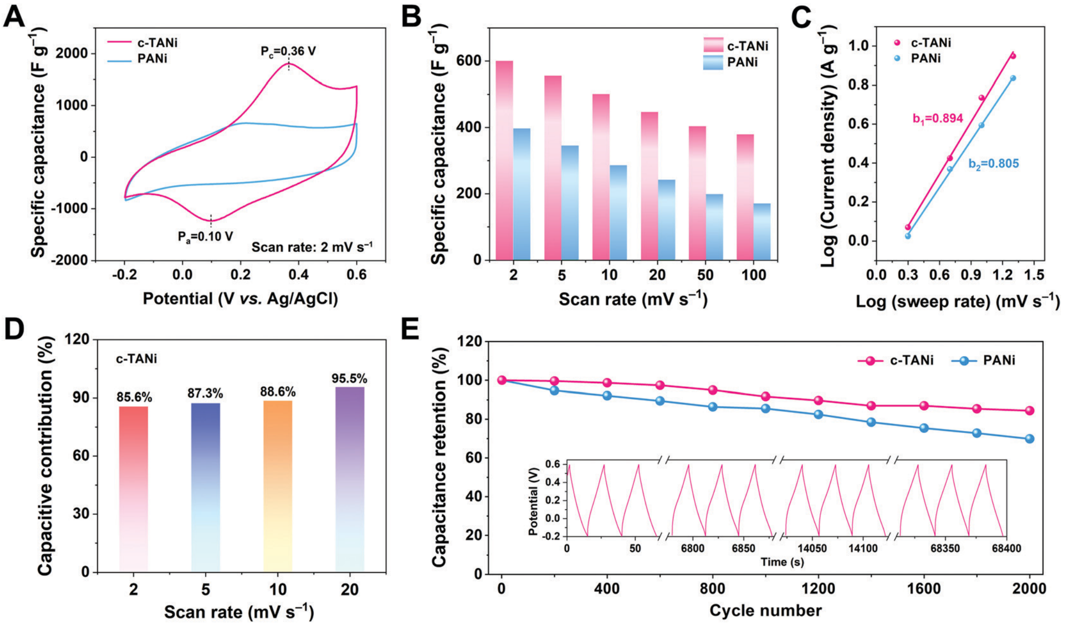

Fig. 2 Electrochemical characterization of the c-TANi electrode. (A) A comparison of CV curves between c-TANi and PANi at a scan rate of 2 mV s^{-1} with a three-electrode configuration in 2.0 M NaCl. (B) Corresponding specific capacitances and (C) *b*-values of c-TANi and PANi obtained at various scan rates. (D) Normalized charge contribution ratio of capacitive capacity at various scan rates. (E) Long-term cycling stability of c-TANi and PANi at a current density of 10 A g^{-1} for 2000 cycles.

Electrochemical impedance spectroscopy (EIS) measurements were further implemented to gain insight into the electrochemical dynamics of the electrodes. As depicted in Fig. S5C (ESI†), we quantitatively evaluated the electronic conductivity and ionic transport properties of c-TANi and PANi electrodes. Clearly, the c-TANi electrode exhibits a lower internal resistance (R_s) of 0.078 Ω compared to the 0.256 Ω observed for PANi. Additionally, the vertical curve displayed in the low frequency region of the Nyquist plot further indicates a favorable ion diffusion efficiency for the c-TANi electrode. The unsatisfactory structural stability leading to moderate electrochemical cycling stability for PANi is one of its crucial weaknesses hindering practical applications. Fig. 2E reveals that the c-TANi electrode delivers a good cycling lifespan of 84.4% after 2000 cycles, while a PANi electrode only retains 69.9% under the same conditions. Overall, these impressive electrochemical performances in an NaCl aqueous electrolyte suggest that c-TANi is a promising electrode in the field of biocompatible electrochemical charge storage devices using physiological electrolytes.

To intuitively elucidate the origins of the outstanding electrochemical performance of c-TANi in a neutral NaCl aqueous electrolyte, the chemical structural evolution during the electrochemical charge/discharge process was systematically investigated using a series of *ex situ* characterization techniques. As depicted in Fig. 3A, Fig. S6A and B (ESI†), *ex situ* X-ray photoelectron spectroscopy (XPS) was first utilized to track the elemental component evolution of the c-TANi electrode. The peaks centered at 199.4 eV and 197.7 eV are referred to as Cl $2p_{1/2}$ and Cl $2p_{3/2}$. Fig. 3B and Table S1 (ESI†) summarize the ratio variations of Cl and Na derived from the high-resolution XPS (Fig. 3A and Fig. S6B, ESI†). The atomic content of Cl gradually increased from 0.4% to 1.15% during the charging process and reversibly fell back upon discharging, while the sodium content remained nearly constant. Based on the extremely low proton concentration, the proton doping/de-doping process is unlikely to contribute any capacity. This is also corroborated by the MALDI-TOF spectrum in which essentially no molecular weight change was observed for each of the selected samples as depicted in Fig. S6C (ESI†). More specifically, the –NH– in the leucoemeraldine state was oxidized to $=NH^+–$ in the emeraldine salt upon charging,[33] accompanied by interactions with Cl^- to preserve electroneutrality. Therefore, we believe that the anion (Cl^-) mediated redox reaction is the essential step contributing to the electrochemical charge storage of c-TANi.

Ex situ XRD in Fig. 3C was also utilized to unravel the crystalline structural variation. From the expanded 2θ range of 15° to 30°, it is evident that the intensity of the peak at 20.8° gradually diminished and then was enhanced from steps I to V. The peak at 25.4° (corresponding to the π–π stacking) strengthened significantly during the charging process, thus illuminating the ordering enhancement of the conjugated structure. To substantiate the molecular structure of c-TANi in the

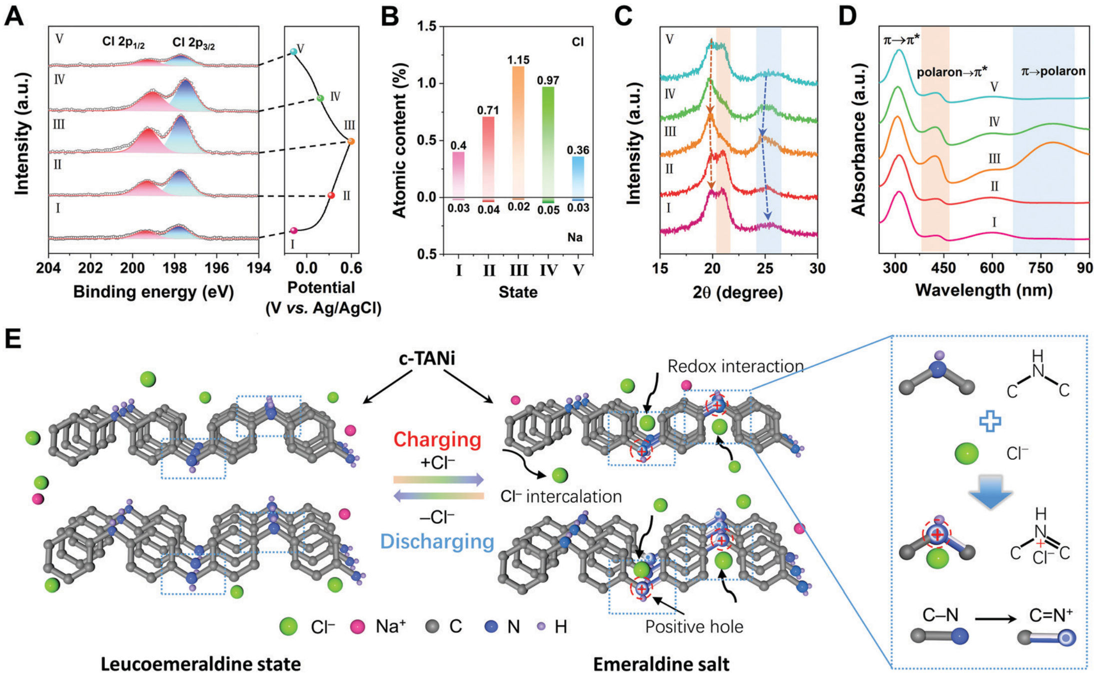

Fig. 3 *Ex situ* characterization for inspecting the charge storage mechanism of c-TANi. (A) Deconvoluted high-resolution evolution of the Cl 2p XPS spectrum and the corresponding GCD curves recorded at a current density of 1 A g^{-1}. The labels from I to V represent the c-TANi samples obtained from the varied charge/discharge steps for the following physical characterizations. (B) Calculated Cl and Na atomic content ratios. (C) XRD patterns and (D) UV-vis spectrum of a c-TANi electrode at different electrochemical steps. (E) Schematic illustration of the charge storage mechanism of c-TANi with redox interactions and Cl^- intercalation, accompanied by c-TANi oxidation state variation between the emeraldine salt and leucoemeraldine oxidation states.

electrochemical process, we deliberately synthesized the leucoemeraldine oxidation state of TANi and the emeraldine base form of TANi, *i.e.*, the de-doped emeraldine oxidation state of TANi. Fig. S6D (ESI†) summarizes the XRD patterns of the leucoemeraldine and the emeraldine base forms of TANi in comparison with its as-prepared c-TANi counterpart, *i.e.*, the proton doped emeraldine salt form. From the XRD profiles of the varied states of TANi (Fig. S6D, ESI†) and *ex situ* XRD curves (Fig. 3C), two hump shaped peaks centered at ~20.0° and 20.8° of the fully discharged samples indicate the leucoemeraldine state of c-TANi, while the charged sample shows a sharp peak located at 19.7° representing the emeraldine salt form of c-TANi. Simultaneously, the peaks centered at 20.0° and 25.6° manifest a conspicuous shift towards lower angles during charging and reversible contraction during discharging, indicative of Cl^- intercalation/de-intercalation accompanied by redox state variations between the emeraldine salt and leucoemeraldine states, as schematically illustrated in Fig. 3E.

Ex situ UV-vis (Fig. 3D) and FT-IR (Fig. S6E, ESI†) results derived from the charged/discharged c-TANi electrodes provide information on the molecular characteristics, redox level and conjugation length. UV-vis absorption peaks located at 311 nm, 425 nm and 800 nm indicate the band structure transitions from $\pi \rightarrow \pi^*$, polaron $\rightarrow \pi^*$ and $\pi \rightarrow$ polaron, respectively.[15,16] Upon charging, the broad peak centered at 800 nm increases remarkably, revealing polaron formation of $=NH^+-$ in the emeraldine salt form. Additionally, the enhanced ratio between the 420 nm peak and the 290 nm peak implies a decrease in the $\pi \rightarrow \pi^*$ transition energy, in the presence of a gradual enhancement of the TANi molecular π–π stacking. These enhanced peaks are gradually reduced or even disappear during the discharging process implying their reversibility. Overall, the series of UV-vis spectra further confirm the structural transition between the emeraldine salt form and the leucoemeraldine state. As demonstrated in the *ex situ* FT-IR spectra in Fig. S6E (ESI†), the peaks centered at 1589 cm^{-1}, 1504 cm^{-1} and 1145 cm^{-1} can be assigned to the stretching vibrations of quinoid (C=Q=C), benzenoid (C=B=C) and benzenoid-NH-quinoid.[34] Upon charging, the ratio enhancement between the C=Q=C and C=B=C indicates an enhancement in the benzenoid-NH-quinoid transition, which also represents an increase in the degree of conjugation.

The uniqueness of the chloride dominated redox reaction and the robust crystalline structure of c-TANi in turn bring about excellent electrochemical performance in an NaCl aqueous electrolyte. As schematically depicted in Fig. 4A, the charge storage mechanism of the c-TANi electrode was investigated in a series of physiological electrolytes with NaCl as the major component, including normal saline (0.9 wt%, *i.e.* 150 mM NaCl), phosphate buffered saline (PBS) solution (1.76 mM KH_2PO_4, 10.1 mM Na_2HPO_4, 136.8 mM NaCl and 2.68 mM KCl) and artificial sweat (85.5 mM NaCl, 16.7 mM urea and 12.7 mM lactic acid). Both c-TANi and PANi electrodes were first investigated with a three-electrode configuration to inspect their intrinsic electrochemical performance. Fig. 4B summarizes the specific capacitance of the c-TANi and PANi

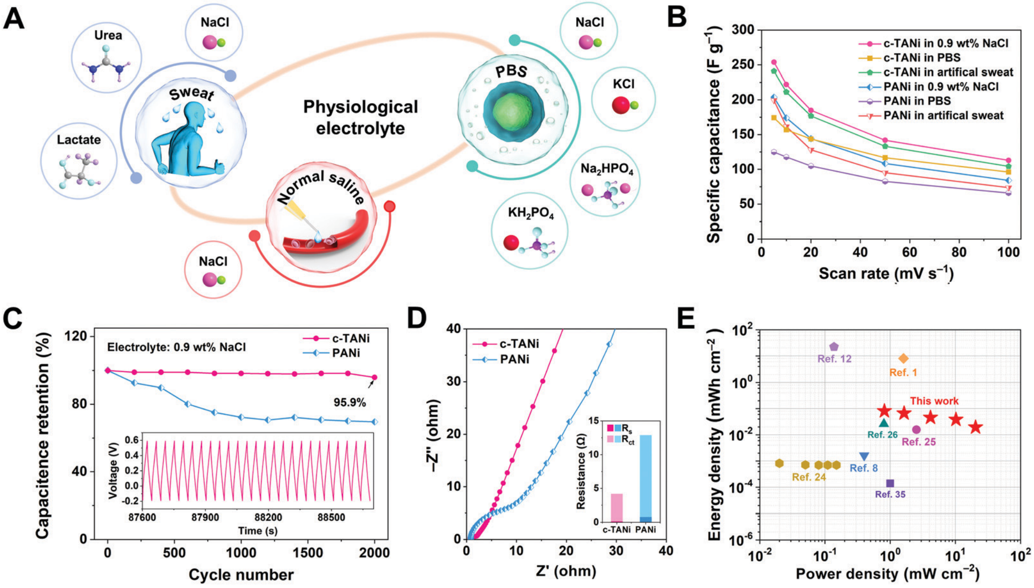

Fig. 4 Electrochemical characterization of c-TANi in physiological electrolytes. (A) A schematical illustration of the c-TANi electrode tested in physiological electrolytes for potential wearable energy storage devices. (B) Summary of specific capacitances of c-TANi and PANi electrodes in normal saline (0.9 wt% NaCl), phosphate buffered saline (PBS) solution and artificial sweat to observe their rate performance in these physiological electrolytes. (C and D) The cycling stability and electrochemical impedance spectroscopy (EIS) comparison between c-TANi and PANi electrodes in saline electrolyte. The inset figure in (D) summarizes the fit of the resistance values of different components in the equivalent circuit. (E) A Ragone plot compares a c-TANi||0.9 wt% NaCl||c-TANi symmetrical supercapacitor reported in this work with other recently published electrochemical charge storage devices in physiological electrolytes, including PEDOT:PSS//artificial sweat,[8] Mg/AgCl//0.35M NaCl,[1] PPy/PEDOT/Mg//0.25 M $Mg(NO_3)_2$,[12] PEDOT:PSS/ferritin/MWCNTs//PBS,[24] MoO_x//sodium alginate,[25] PANI/CNT//1.0 M NaCl,[26] and MoO_3//0.35 M NaCl.[3]

electrodes in all three types of physiological electrolytes with varied sweep rates according to the CV curves presented in Fig. S7 (ESI†). Overall, the c-TANi electrode exhibited a superior specific capacitance compared to the PANi electrode in all three types of physiological electrolytes. In normal saline with a 0.9 wt% NaCl, the c-TANi electrode exhibited a superior specific capacitance of 254.6 F g^{-1} at a scan rate of 5 mV s^{-1}, in comparison to 203.8 F g^{-1} for the PANi electrode at the coincident scan rate. As can be seen in Fig. S8A (ESI†), the c-TANi electrode exhibited similar CV profile shapes to the corresponding results acquired in a 2.0 M NaCl aqueous electrolyte. This is indicative of the analogous redox active Cl^- intercalation charge storage mechanism for c-TANi even at such a low NaCl concentration (0.15 M). Additionally, the c-TANi electrode also exhibited acceptable specific capacitances of 240.9 and 174.2 F g^{-1} in artificial sweat and PBS electrolytes, respectively, which both exceed the specific capacitances of 199.2 F g^{-1} and 124.9 F g^{-1} obtained with a PANi electrode. The slight specific capacitance decline for the c-TANi electrode in artificial sweat and the PBS electrolytes, is likely due to the lower ion concentration (0.085 M in artificial sweat, 0.14 M in PBS), complex composition of artificial sweat (85.5 mM NaCl, 16.7 mM urea and 12.7 mM lactic acid) and PBS (1.76 mM KH_2PO_4, 10.1 mM Na_2HPO_4, 137 mM NaCl and 2.68 mM KCl). Note that the c-TANi electrode also exhibits good rate stability of 44.3% (in normal saline), 43.3% (in artificial sweat) and 55.2% (in PBS) capacitance retention even as the scan rate was increased to 100 mV s^{-1}. Meanwhile, excellent rate capacitance retention can also be observed in GCD curves (Fig. S9, ESI†). As seen in Fig. 4C, the c-TANi electrode also provided significantly better cycling stability of 95.9% compared to 69.9% for PANi after 2000 cycles under consistent measurement conditions in a normal saline electrolyte. Such a significant increase in capacitance retention can be further demonstrated in artificial sweat (94.1%) and PBS (82.5%) electrolytes, which is far superior to that of 20.2% and 12.2%, respectively, obtained with PANi electrode (Fig. S10A, ESI†). To gain full insight into the ionic dynamics of the enhanced electrochemical performance of the c-TANi electrode, the EIS spectrum was further used to characterize the charge transfer and ion diffusion resistance. Fig. 4D and Fig. S8B (ESI†) in 0.9 wt% NaCl electrolyte display the Nyquist plots for the c-TANi and PANi electrodes, respectively, while a summary of the resistance values derived from the equivalent circuit simulation is presented in Table S2 (ESI†). The c-TANi electrode exhibits an intrinsic resistance (R_s) of 0.16 Ω and a charge transfer resistance (R_{ct}) of 4.0 Ω, which is superior to the 0.82 Ω and 12.1 Ω observed with the PANi electrode. Furthermore, the c-TANi electrode in 0.9 wt% NaCl presents a higher R_{ct} than that in artificial sweat and PBS electrolytes. Such a result can be attributed to the higher Cl^- concentration and the alkaline nature of PBS (pH = 7.4), which may trigger the de-doping of c-TANi, thus decreasing the conductivity. To further elucidate the cycling stability of the c-TANi electrode in a saline electrolyte, structural characterization, including SEM, UV-vis and FT-IR, for the cycled c-TANi and PANi electrodes were performed. Fig. S11 (ESI†) presents the SEM images of the c-TANi and PANi electrodes after long-term (2000) cycles. The c-TANi electrode presents homogeneous integrity in its morphology, in comparison to observable fractures and electrochemical corrosion of its PANi electrode counterpart. The FT-IR spectra of the PANi electrode (Fig. S12A, ESI†) exhibits a noticeable peak at 1624 cm^{-1} that can be assigned to the stretching vibration of the imide group of oligoaniline, which is indicative of serious structural degradation of PANi after long-term electrochemical cycling.[34] In contrast, the FT-IR spectrum of c-TANi remained essentially unchanged even after 2000 electrochemical cycles (Fig. S12B, ESI†). UV-vis spectra (Fig. S12C and S12D, ESI†) further substantiated the chemical structural evolution of the c-TANi and PANi electrodes after long-term cycling. Intrinsic PANi is almost insoluble in acetonitrile, consistent with its weak absorption signal in the UV-vis spectra.[34] However, PANi extracted from the electrode after long-term cycling exhibits a sharp peak at 230 nm and broad peaks centered at 270 nm and 487 nm, indicating the formation of heterogeneous oligoanilines due to electrochemical degradation.

To demonstrate the advantages of c-TANi in a physiological electrolyte towards creating a biocompatible energy storage device, a symmetric supercapacitor with c-TANi electrodes in a saline electrolyte was investigated. Fig. S13A (ESI†) shows the CV curves at scan rates ranging from 5 mV s^{-1} to 100 mV s^{-1}. Note the remarkable redox active peaks at slow scan rates that shrink into spindle shapes upon accelerating the sweep rate. The supercapacitor displayed an areal capacitance of 413.7 mF cm^{-2} at a sweep rate of 5 mV s^{-1} and preserved 44% of its capacitance when the sweep rate was increased to 100 mV s^{-1} (Fig. S13B, ESI†). A supercapacitor with a saline electrolyte maintained 94.5% capacitance even after 4000 long-term cycles with a current density of 10 A g^{-1} (Fig. S13E, ESI†). This transcends all previously reported electrochemical charge storage devices with physiological electrolytes.[6,8,10,12,23–26] A Ragone plot (Fig. 4E) provides an energy density and power density comparison between the biocompatible c-TANi//saline electrolyte symmetric supercapacitor and other previously reported biocompatible energy storage devices with physiological electrolytes. The c-TANi//saline electrolyte symmetric supercapacitor exhibits an areal energy density of 80.3 μW h cm^{-2} with a power density of 0.82 mW cm^{-2}, which surpasses current state-of-the-art systems such as 0.82 μW h cm^{-2} for a PEDOT:PSS/ferritin//MWNT (PBS) cell,[24] 15.64 μW h cm^{-2} for a MoO_x//MoO_x (sodium alginate) cell,[25] 0.14 μW h cm^{-2} for a MoO_3//MoO_3 (0.35 M NaCl) cell,[35] 1.63 μW h cm^{-2} for a PEDOT:PSS//PEDOT:PSS (artificial sweat) cell[8] and 26 μW h cm^{-2} for a PANi/CNT//PANi/CNT (1.0 M NaCl) cell.[26] To guarantee the full biocompatibility of the supercapacitor, we also tested the cytotoxicity of c-TANi by recording the viability of L929 cells *via* culturing on the surface of c-TANi in Dulbecco's modified Eagle's medium (DMEM) after 72 h. As depicted in Fig. S14 and S15 (ESI†), the cell viability test verifies the good biocompatibility of the c-TANi electrode. The long cycling lifespan, high energy density and superior rate performance of the c-TANi//saline electrolyte supercapacitor make it a promising

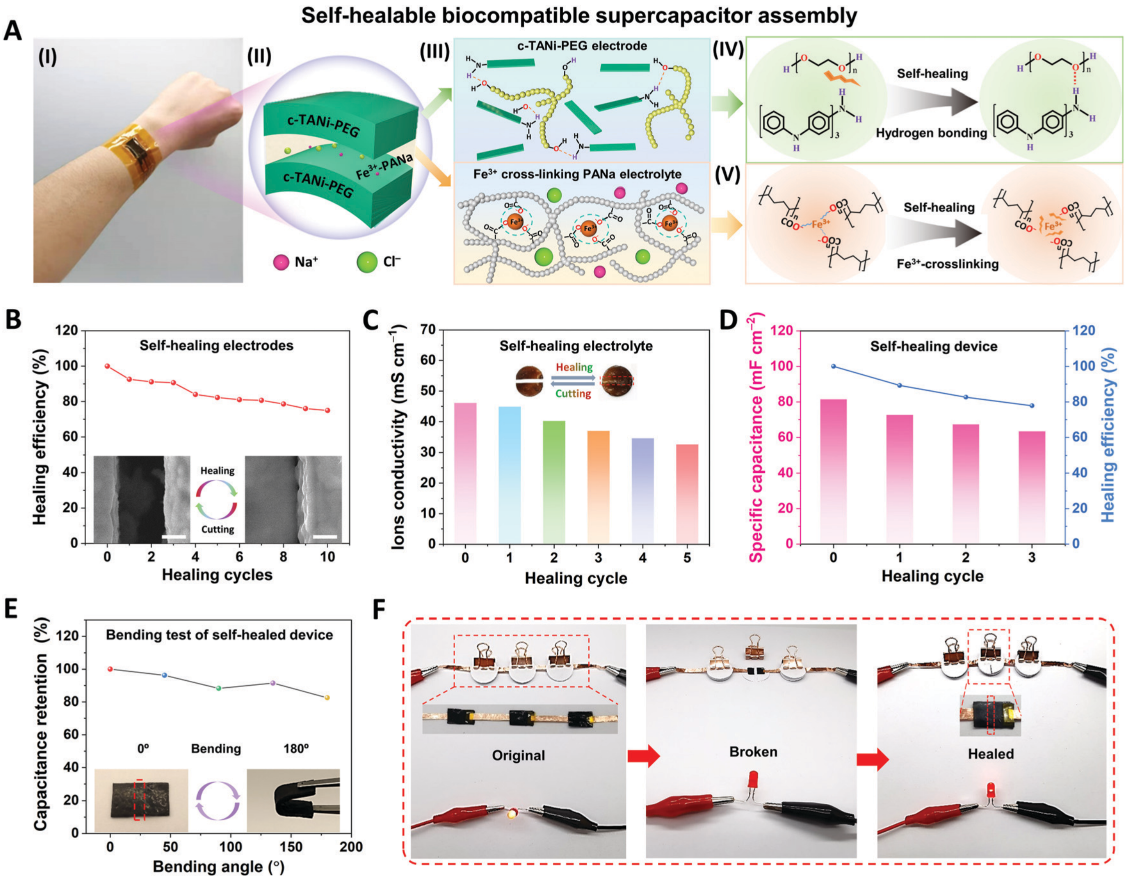

Fig. 5 Fabrication of c-TANi based biocompatible and self-healable quasi-solid-state supercapacitor and its self-healing capability. (A) Illustration of a biocompatible and self-healable c-TANi based supercapacitor and the schematic illustration of the self-healing process for the full device including electrode and gel electrolyte. (B) Healing cycling stability of the c-TANi-PEG electrode over 10 cycles. The healing efficiency calculated by the capacitance retention from both CV and GCD measurements. (C) Ionic conductivity of the Fe^{3+}-PANa gel electrolyte cut and healed over 5 cycles. (D) Areal capacitance retention and healing efficiency of the full c-TANi based biocompatible and self-healable supercapacitor. (E) Capacitance retention of the self-healing supercapacitor at different bending angles. (F) Optical images showing the cut and healing process for three supercapacitors connected in series to power an LED.

candidate for use as a real biocompatible electrochemical charge storage device.

Due to repeated configurational deformations accompanied by the electrochemical cycling process, wearable energy storage devices unavoidably suffer from structural damage between different functional layers, such as cracks, crazing and delamination, which may result in serious performance degradation and even safety issues.[5] Inspired by biological tissue, self-healing features have been found to be a useful strategy to address these issues by restoring the original electrode or full device. Thus, here we integrate the c-TANi electrode with self-healing capabilities by incorporating c-TANi with polyethylene glycol 2000 (PEG-2000) to build a reversible hydrogen bonding enabled self-healing electrode. Additionally, we also construct a ferric-ion cross-linking sodium polyacrylate (Fe^{3+}-PANa)/0.9 wt% NaCl gel electrolyte to establish a synchronous self-healing functionality for both electrode and gel electrolyte. Fig. 5A illustrates the configuration, composition and self-healing mechanism of a c-TANi-PEG electrode with a Fe^{3+}-PANa/0.9 wt% NaCl gel electrolyte. As depicted in Fig. 5A (IV), the PEG chains contribute ample hydroxy groups within the c-TANi-PEG electrode, which can functionalize with the amino or imino groups on the c-TANi to form acceptors and donors for reversible hydrogen-bond self-healing. The PEG chains can also serve as a soft matrix for the flexible and healable electrode, which favors diffusion towards the malfunctioning area. Fig. S16A (I) and Fig. S16B (ESI†) indicate the great flexibility and softness of c-TANi-PEG film with an elongation at break of ~10% upon application of a stress of ~630 kPa. Additionally, the Fe^{3+}-PANa electrolyte consists of a physical cross-linked network with ferric ion-enhanced ionic interactions between the polymer chains. The polarized lone electron pairs on the oxygen atoms of the carboxyl groups in the PANa chains trigger the ionic cross-linking interactions with the electropositive ferric ions (Fig. 5A (V)). When the crosslinking interactions are damaged, they can be re-established with the incorporation of Fe^{3+} ions. In this regard, c-TANi-PEG combined with the Fe^{3+}-PANa electrolyte endows the supercapacitor with an all-self-healing capability.

The self-healing capabilities of the electrode and gel electrolyte were first characterized separately. The c-TANi-PEG electrode was cut into two pieces which were then put closely together and exposed to infrared radiation for 60 min to achieve full healing (Fig. S16 A(III), ESI†). As depicted in the inset SEM images to Fig. 5B, there are no discernible interstices between the two sides after healing. FT-IR spectroscopy (Fig. S16C, ESI†) has been implemented to characterize the chemical structure variation after infusing c-TANi with PEG. The appreciable peak enhancement centered at 2880 cm^{-1} for c-TANi-PEG corresponds to the C–H stretching of PEG, signifying the successful linking of PEG to the c-TANi nanosheets.[36] The distinct broad peak at 3433 cm^{-1} is ascribed to the symmetrical stretching vibration of the –OH groups, which is sensitive to hydrogen bonding.[15,37,38] In contrast to the pure c-TANi and PEG, the –OH stretching peak of c-TANi-PEG is increased, indicating the presence of hydrogen bonding interactions between the hydroxyl groups on the PEG and c-TANi molecular chains.[37] The hydrogen bonded functional groups offer reversible hydrogen bonding to achieve a favorable self-healing electrode. Upon damage to the c-TANi-PEG film, the reversible hydrogen bonds broke. After exposure to infrared radiation (IR), the movement of PEG chains facilitates the chain mobility on the damaged interface, thus the hydrogen bonds can be reconstructed and self-healing occurs.

The healing efficiency of the c-TANi-PEG electrode was evaluated using both specific capacitance and electronic conductivity preservation after 10 repeated cutting and healing cycles. As presented in Fig. S16D and E (ESI†), the c-TANi-PEG electrode displayed an initial electronic conductivity of 0.66 mS cm^{-1} and maintained 40.9% of its conductivity after 10 cut/healing cycles. Fig. S17B (ESI†) displays the specific capacitance of the c-TANi-PEG electrode as calculated from the GCD profile (Fig. S17A, ESI†) after every cut/healing cycle. The c-TANi-PEG electrode delivers a 75.0% capacitance retention (Fig. 5B), *i.e.*, healing efficiency, after 10 cycles compared to its original areal capacitance of 131.9 mF cm^{-2} (Fig. S17B, ESI†).

Meanwhile, the as-prepared Fe^{3+}-PANa gel electrolyte exhibited an excellent ionic conductivity of 46.1 mS cm^{-1} even in a saline electrolyte (Fig. 5C). A remarkable stretchability up to 162% with a tensile stress of 76.8 kPa (Fig. S18B, ESI†) was measured. The inset image in Fig. 5C and the optical image in Fig. S18A (ESI†) demonstrates that the self-healing Fe^{3+}-PANa gel electrolyte can restore its structural integrity and even carry a 50 g weight. As depicted in Fig. S18C (ESI†), the healing stability has also been characterized by 5 repeated cut/healing cycles, with a 70.9% ionic conductivity preservation. The final healed electrode still maintained a reversible elongation of 150% and a tensile stress of 73.3 kPa.

Finally, a flexible supercapacitor with all-self-healing capability has been assembled by utilizing c-TANi-PEG as the electrodes and Fe^{3+}-PANa/normal saline as the gel electrolyte. The thus-manufactured supercapacitor delivered an areal capacitance of 81.5 mF cm^{-2} and a self-healing efficiency of 77.8% after three cutting/healing cycles (Fig. 5D). The interfacial structural robustness between the electrode and gel electrolyte is another vital factor determining the performance of the full self-healing supercapacitor. Therefore, EIS spectroscopy was used to investigate the electrochemical interfacial evolution (Fig. S19B, ESI†) after each cutting/healing cycle. As summarized in Table S4 (ESI†), the intrinsic resistance (R_s) increased from 5.0 Ω to 11.1 Ω, while the charge transfer resistance (R_{ct}) only went up from 38.2 Ω to 49.2 Ω after 3 cutting/healing cycles, indicative of an acceptable electronic and ionic resistance variation even after multi-healing cycles. More encouragingly, the manufactured c-TANi based biocompatible supercapacitor exhibited considerable flexibility even after multiple cutting/healing cycles. Fig. 5E and Fig. S20A (ESI†) show 82.4% capacitance preservation with bending angle variations from 0 to 180° at a radius of curvature ∼5 mm. Furthermore, the stable electrochemical behavior is indicated by the constant brightness over 8 min of a light-emitting diode (LED) powered by the biocompatible supercapacitor as can be seen in Fig. S21 (ESI†). In addition, a light-emitting diode (LED) also can be powered by the healed biocompatible supercapacitor even after the 1st cutting/healing cycle (Fig. 5F). The remarkable self-healing capability of the full supercapacitor mainly lies in the synchronously self-healing effect for both the c-TANi-PEG electrode and the Fe^{3+}-PANa gel electrolyte.

Conclusions

In summary, we have demonstrated a new strategy to construct a biocompatible and flexible supercapacitor by utilizing c-TANi as the electrodes and physiological liquids as electrolytes. By virtue of the intrinsic crystallinity and improved conductivity, c-TANi electrodes exhibit remarkably enhanced specific capacitance and cycling stability even in a normal saline physiological electrolyte, compared with a PANi electrode. The Cl^{-} anion dominant intercalation redox charge storage mechanism mainly contributes to the promoted capacitance, which has been systematically studied with a series of *ex situ* characterization techniques. After grafting with a PEG polymer matrix, the c-TANi electrode is endowed with great self-healing capability thanks to abundant hydrogen bonding from amino groups on the c-TANi and hydroxyl groups on the PEG. An all-polymer self-healing and biocompatible supercapacitor was assembled by taking advantage of the self-healing c-TANi-PEG electrode and an Fe^{3+}-PANa/0.9 wt% NaCl gel electrolyte, which exhibited a 77.8% capacitance retention even after three cut/healing cycles. Such self-healing biocompatible supercapacitors offer novel insights into envisioning high-energy, long-life and safe energy storage devices that can power wearable or even implantable medical devices.

Conflicts of interest

The authors declare no competing financial interest.

Acknowledgements

This project was financially supported by: a start-up research grant for a distinguished professor at Soochow University

(Y. S.), the National Natural Science Foundation of China No. 52003188 (Y. S.), the Natural Science Foundation of Jiangsu Province No. BK20200871 (Y. S.), open research fund for Jiangsu Provincial Key Laboratory for Advanced Carbon Materials and Wearable Energy Technologies (Y. S.), open research fund State Key Laboratory for Modification of Chemical Fibers and Polymer Materials, Donghua University No. KF2104 (Y. S.). R. B. K. thanks the Dr. Myung Ki Hong Endowed Chair in Materials Innovation at UCLA. Y. Z. acknowledges the financial support from the National Natural Science Foundation of China (Grant No. 21771161 and 51701181) and the Zhejiang Provincial Natural Science Foundation of China (Grant No. LR18B030003).

Notes and references

1 A. J. Bandodkar, S. P. Lee, I. Huang, W. Li, S. Wang, C. J. Su, W. J. Jeang, T. Hang, S. Mehta, N. Nyberg, P. Gutruf, J. Choi, J. Koo, J. T. Reeder, R. Tseng, R. Ghaffari and J. A. Rogers, *Nat. Electron.*, 2020, **3**, 554–562.

2 T. Wang, M. Wang, L. Yang, Z. Li, X. J. Loh and X. Chen, *Adv. Mater.*, 2020, **32**, 1905522.

3 H. L. Park, Y. Lee, N. Kim, D. G. Seo, G. T. Go and T. W. Lee, *Adv. Mater.*, 2020, **32**, 1903558.

4 J. Li, J. Zhao and J. A. Rogers, *Acc. Chem. Res.*, 2019, **52**, 53–62.

5 X. L. Tong, Z. N. Tian, J. Y. Sun, V. C. Tung, R. B. Kaner and Y. L. Shao, *Mater. Today*, 2021, **44**, 78–104.

6 Z. Guo, Y. Zhao, Y. Ding, X. Dong, L. Chen, J. Cao, C. Wang, Y. Xia, H. Peng and Y. Wang, *Chem*, 2017, **3**, 348–362.

7 Z. Tian, X. Tong, G. Sheng, Y. Shao, L. Yu, V. Tung, J. Sun, R. B. Kaner and Z. Liu, *Nat. Commun.*, 2019, **10**, 4913.

8 L. Manjakkal, A. Pullanchiyodan, N. Yogeswaran, E. S. Hosseini and R. Dahiya, *Adv. Mater.*, 2020, **32**, 1907254.

9 F. Gschwind, H. Euchner and G. Rodriguez-Garcia, *Eur. J. Inorg. Chem.*, 2017, 2784–2799.

10 J. Hur, K. Im, S. W. Kim, U. J. Kim, J. Lee, S. Hwang, J. Song, S. Kim, S. Hwang and N. Park, *J. Mater. Chem. A*, 2013, **1**, 14460–14466.

11 S. Zhang, Y. Chen, H. Liu, Z. Wang, H. Ling, C. Wang, J. Ni, B. Celebi-Saltik, X. Wang, X. Meng, H. J. Kim, A. Baidya, S. Ahadian, N. Ashammakhi, M. R. Dokmeci, J. Travas-Sejdic and A. Khademhosseini, *Adv. Mater.*, 2020, **32**, 1904752.

12 C. Yu, C. Wang, X. Liu, X. Jia, S. Naficy, K. Shu, M. Forsyth and G. G. Wallace, *Adv. Mater.*, 2016, **28**, 9349–9355.

13 H. Li, J. Wang, Q. Chu, Z. Wang, F. Zhang and S. Wang, *J. Power Sources*, 2009, **190**, 578–586.

14 J. Liu, Y. S. Kim, C. E. Richardson, A. Tom, C. Haru Ramakrishnan, F. Birey, T. Katsumata, S. Chen, C. Wang, X. Wang, L.-M. Joubert, Y. Jiang, H. Wang, L. E. Fenno, J. B.-H. Tok, S. P. Paşca, K. Shen, Z. Bao and K. Deisseroth, *Science*, 2020, **367**, 1372–1376.

15 Y. Wang, H. D. Tran, L. Liao, X. Duan and R. B. Kaner, *J. Am. Chem. Soc.*, 2010, **132**, 10365–10373.

16 Y. Wang, J. Liu, H. D. Tran, M. Mecklenburg, X. N. Guan, A. Z. Stieg, B. C. Regan, D. C. Martin and R. B. Kaner, *J. Am. Chem. Soc.*, 2012, **134**, 9251–9262.

17 Y. Wang, J. A. Torres, A. Z. Stieg, S. Jiang, M. T. Yeung, Y. Rubin, S. Chaudhuri, X. Duan and R. B. Kaner, *ACS Nano*, 2015, **9**, 9486–9496.

18 T. Zhang, H. Qi, Z. Liao, Y. D. Horev, L. A. Panes-Ruiz, P. S. Petkov, Z. Zhang, R. Shivhare, P. Zhang, K. Liu, V. Bezugly, S. Liu, Z. Zheng, S. Mannsfeld, T. Heine, G. Cuniberti, H. Haick, E. Zschech, U. Kaiser, R. Dong and X. Feng, *Nat. Commun.*, 2019, **10**, 4225.

19 I. Y. Choi, J. Lee, H. Ahn, J. Lee, H. C. Choi and M. J. Park, *Angew. Chem., Int. Ed.*, 2015, **54**, 10497–10501.

20 Y. Yan, R. Wang, X. Qiu and Z. Wei, *J. Am. Chem. Soc.*, 2010, **132**, 12006–12012.

21 Z. Wei, T. Laitinen, B. Smarsly, O. Ikkala and C. F. Faul, *Angew. Chem., Int. Ed.*, 2005, **44**, 751–756.

22 O. A. Bell, G. Wu, J. S. Haataja, F. Brommel, N. Fey, A. M. Seddon, R. L. Harniman, R. M. Richardson, O. Ikkala, X. Zhang and C. F. Faul, *J. Am. Chem. Soc.*, 2015, **137**, 14288–14294.

23 J. S. Chae, N.-S. Heo, C. H. Kwak, W.-S. Cho, G. H. Seol, W.-S. Yoon, H.-K. Kim, D. J. Fray, A. T. E. Vilian, Y.-K. Han, Y. S. Huh and K. C. Roh, *Nano Energy*, 2017, **34**, 86–92.

24 H. J. Sim, C. Choi, D. Y. Lee, H. Kim, J.-H. Yun, J. M. Kim, T. M. Kang, R. Ovalle, R. H. Baughman, C. W. Kee and S. J. Kim, *Nano Energy*, 2018, **47**, 385–392.

25 H. Sheng, J. Zhou, B. Li, Y. He, X. Zhang, J. Liang, J. Zhou, Q. Su, E. Xie, W. Lan, K. Wang and C. Yu, *Sci. Adv.*, 2021, **7**, eabe3097.

26 Z. Luo, Y. Wang, B. Kou, C. Liu, W. Zhang and L. Chen, *Energy Storage Mater.*, 2021, **38**, 9–16.

27 C. W. Lin, S. Aguilar, E. Rao, W. H. Mak, X. Huang, N. He, D. Chen, D. Jun, P. A. Curson, B. T. McVerry, E. M. V. Hoek, S. C. Huang and R. B. Kaner, *Chem. Sci.*, 2019, **10**, 4445–4457.

28 K. Lee, S. Cho, S. H. Park, A. J. Heeger, C. W. Lee and S. H. Lee, *Nature*, 2006, **441**, 65–68.

29 K. Balakrishnan, A. Datar, R. Oitker, H. Chen, J. Zuo and L. Zang, *J. Am. Chem. Soc.*, 2005, **127**, 10496–10497.

30 C. O. Baker, X. Huang, W. Nelson and R. B. Kaner, *Chem. Soc. Rev.*, 2017, **46**, 1510–1525.

31 Y. Wang, X. Yang, L. Qiu and D. Li, *Energy Environ. Sci.*, 2013, **6**, 477–481.

32 S. Ardizzone, G. Fregonara and S. Trasatti, *Electrochim. Acta*, 1990, **35**, 263–267.

33 F. Wan, L. Zhang, X. Wang, S. Bi, Z. Niu and J. Chen, *Adv. Funct. Mater.*, 2018, **28**, 1804975.

34 Q. Zhang, A. Zhou, J. Wang, J. Wu and H. Bai, *Energy Environ. Sci.*, 2017, **10**, 2372–2382.

35 G. Lee, S.-K. Kang, S. M. Won, P. Gutruf, Y. R. Jeong, J. Koo, S.-S. Lee, J. A. Rogers and J. S. Ha, *Adv. Energy Mater.*, 2017, **7**, 1700157.

36 Y. Li, X. Li, S. Zhang, L. Liu, N. Hamad, S. R. Bobbara, D. Pasini and F. Cicoira, *Adv. Funct. Mater.*, 2020, **30**, 2002853.

37 G. Cai, J. Wang, K. Qian, J. Chen, S. Li and P. S. Lee, *Adv. Sci.*, 2017, **4**, 1600190.

38 L. Ma, S. Chen, D. Wang, Q. Yang, F. Mo, G. Liang, N. Li, H. Zhang, J. A. Zapien and C. Zhi, *Adv. Energy Mater.*, 2019, **9**, 1803046.